

Rydberg-positronium velocity and self-ionization studies in a 1T magnetic field and cryogenic environment

M. Antonello,^{1,2} A. Belov,³ G. Bonomi,^{4,5} R. S. Brusa,^{6,7} M. Caccia,^{1,2} A. Camper,^{8,*} R. Caravita,⁷ F. Castelli,^{1,9} D. Comparat,¹⁰ G. Consolati,^{11,1} L. Di Noto,^{12,13} M. Doser,⁸ M. Fani,^{12,13,8} R. Ferragut,^{14,1} J. Fesel,⁸ S. Gerber,⁸ A. Gligorova,¹⁵ L. T. Glöggler,⁸ F. Guatieri,^{6,7} S. Haider,⁸ A. Hinterberger,⁸ O. Khalidova,⁸ D. Krasnický,¹³ V. Lagomarsino,^{12,13} C. Malbrunot,⁸ S. Mariazzi,^{6,7} V. Matveev,^{3,16} S. R. Müller,¹⁷ G. Nebbia,¹⁸ P. Nedelec,¹⁹ L. Nowak,⁸ M. Oberthaler,¹⁷ E. Oswald,⁸ D. Pagano,^{4,5} L. Penasa,^{6,7} V. Petracek,²⁰ F. Prelz,¹ B. Rienäcker^{8,†} O. M. Røhne,²¹ A. Rotondi,^{5,22} H. Sandaker,²¹ R. Santoro,^{1,2} G. Testera,¹³ I. C. Tietje,⁸ T. Wolz,⁸ C. Zimmer,^{8,21,23} and N. Zurlo^{5,24}
(AEgIS Collaboration)

¹INFN, Sezione di Milano, via Celoria 16, 20133 Milano, Italy

²Department of Science and High Technology, University of Insubria, Via Valleggio 11, 22100 Como, Italy

³Institute for Nuclear Research of the Russian Academy of Science, Moscow 117312, Russia

⁴Department of Mechanical and Industrial Engineering, University of Brescia, via Branze 38, 25123 Brescia, Italy

⁵INFN Pavia, via Bassi 6, 27100 Pavia, Italy

⁶Department of Physics, University of Trento, via Sommarive 14, 38123 Povo, Trento, Italy

⁷TIFPA/INFN Trento, via Sommarive 14, 38123 Povo, Trento, Italy

⁸Physics Department, CERN, 1211 Geneva 23, Switzerland

⁹Department of Physics “Aldo Pontremoli”, Università degli Studi di Milano, via Celoria 16, 20133 Milano, Italy

¹⁰Laboratoire Aimé Cotton, Université Paris-Sud, ENS Paris Saclay, CNRS, Université Paris-Saclay, 91405 Orsay Cedex, France

¹¹Department of Aerospace Science and Technology, Politecnico di Milano, via La Masa 34, 20156 Milano, Italy

¹²Department of Physics, University of Genova, via Dodecaneso 33, 16146 Genova, Italy

¹³INFN Genova, via Dodecaneso 33, 16146 Genova, Italy

¹⁴LNESS, Department of Physics, Politecnico di Milano, via Anzani 42, 22100 Como, Italy

¹⁵Stefan Meyer Institute for Subatomic Physics, Austrian Academy of Sciences, Boltzmanngasse 3, 1090 Vienna, Austria

¹⁶Joint Institute for Nuclear Research, Dubna 141980, Russia

¹⁷Kirchhoff-Institute for Physics, Heidelberg University, Im Neuenheimer Feld 227, 69120 Heidelberg, Germany

¹⁸INFN Padova, via Marzolo 8, 35131 Padova, Italy

¹⁹Institute of Nuclear Physics, CNRS/IN2p3, University of Lyon 1, 69622 Villeurbanne, France

²⁰Czech Technical University, Prague, Břehová 7, 11519 Prague 1, Czech Republic

²¹Department of Physics, University of Oslo, Sem Saelandsvei 24, 0371 Oslo, Norway

²²Department of Physics, University of Pavia, via Bassi 6, 27100 Pavia, Italy

²³Department of Physics, Heidelberg University, Im Neuenheimer Feld 226, 69120 Heidelberg, Germany

²⁴Department of Civil, Environmental, Architectural Engineering and Mathematics, University of Brescia, via Branze 43, 25123 Brescia, Italy



(Received 7 February 2020; accepted 11 May 2020; published 2 July 2020)

We characterized the pulsed Rydberg-positronium production inside the Antimatter Experiment: Gravity, Interferometry, Spectroscopy (AEgIS) apparatus in view of antihydrogen formation by means of a charge exchange reaction between cold antiprotons and slow Rydberg-positronium atoms. Velocity measurements on the positronium along two axes in a cryogenic environment (≈ 10 K) and in 1 T magnetic field were performed. The velocimetry was done by microchannel-plate (MCP) imaging of a photoionized positronium previously excited to the $n = 3$ state. One direction of velocity was measured via Doppler scan of this $n = 3$ line, another direction perpendicular to the former by delaying the exciting laser pulses in a time-of-flight measurement. Self-ionization in the magnetic field due to the motional Stark effect was also quantified by using the same MCP-imaging technique for Rydberg positronium with an effective principal quantum number n_{eff} ranging between 14 and 22. We conclude with a discussion about the optimization of our experimental parameters for creating Rydberg positronium in preparation for an efficient pulsed production of antihydrogen.

DOI: [10.1103/PhysRevA.102.013101](https://doi.org/10.1103/PhysRevA.102.013101)

*antoine.camper@cern.ch

†benjamin.rienaecker@cern.ch

The positronium excitation is achieved by two synchronized and superimposed laser pulses. The first one enabling the $1^3S \rightarrow 3^3P$ transition is a 1.5 ns-long UV pulse, tunable from (204.9–205.2) nm at $43\mu\text{J}$ with a bandwidth of 118 GHz. The second is for the transition to Rydberg states, namely, an IR pulse, 3 ns long and tunable from (1671–1715) nm at 1.6 mJ with a bandwidth of 430 GHz. In addition, a 1064 nm IR pulse at 30 mJ can be delivered in order to selectively photoionize all Ps in the 3^3P state. The positron [25] and laser [20] systems are described in detail elsewhere.

The electrodes of the antihydrogen production trap, placed below the Ps-excitation area and partially visible in Fig. 1, allow one to store antiprotons during the procedure. The maximum antihydrogen production within the magnetic field \vec{B} (parallel to the z axis) will be achieved by steering the highest Rydberg-Ps flux originating from the target towards that trap, and by optimizing the Ps state as well as the laser-selected Ps velocity regime in the x - y plane. At the top of these trap electrodes is an opening covered by a meshed grid which allows Ps to enter. The exciting laser pulses are aligned parallel to the positron-to-Ps converter target, and thus along the y axis. In Fig. 1, we indicate the position of the UV and IR laser beams which was used throughout the whole presented measurement series. A MACOR-screen (a white machinable glass-ceramic sold by Corning, Inc., which is fit for cryo- and UHV environments) has been placed in the target's proximity in the x - z plane with the purpose to image laser pulses and monitor their position, as was already done in Ref. [20]. For the measurements presented here, the central position of the laser was set to -3.2 mm in the z direction and 1.7 mm in the x direction from the lower edge of the target.

The laser timing was referenced to the prompt annihilation peak of implanted positrons, which we defined as $t = 0$. For this, the positron annihilation radiation was detected with scintillator slabs (EJ200) coupled to a photomultiplier tube (PMT). Additionally, we acquired the electric signal on the MCP frontface, which was generated immediately after irradiation with scattered UV light. Both the positron peak and the laser peak were absolutely calibrated to each other, as described in Ref. [26]. Using the MCP-imaging technique, a single image could be acquired for one specific setting at the same repetition rate as the AEGIS positron system that was delivering positron bunches, namely, 1 minute per bunch. If a setting was repeated up to five times, a full measurement series required approximately 5×60 different settings \times 1 min = 300 min.

The characterization of the Ps-velocity profiles and the fraction of Rydberg-Ps surviving self-ionization were studied by performing three different types of experimental procedures: (i) timing scans, (ii) Doppler scans, and (iii) Rydberg self-ionization scans.

(i) The timing scans focused on the determination of the Ps-velocity component aligned with the vertical x axis by means of photoionization of Ps atoms via a two-step optical transition and a subsequent measurement of the intensity distribution of released positrons. The timing scans were performed by changing the delay between positron implantation into the target and the trigger for laser excitation. Delays from -5 ns up to 265 ns were applied to both the UV pulse exciting Ps via

$1^3S \rightarrow 3^3P$, operating at resonance ($\lambda = 205.045$ nm, taken as a reference in the following), and to the IR pulse at 1064 nm in order to selectively photoionize the fraction of Ps in the $n = 3$ state. This fraction goes up to 15% of the whole Ps cloud being emitted into vacuum [20]. The released photopositrons were guided by the homogeneous 1 T magnetic field towards a microchannel plate coupled to a phosphor screen (MCP Hamamatsu F2223+ Phosphor screen P46) and imaged by this assembly [21]. The frontface of the MCP was biased to -180 V, and the gain voltage between the two stages of the MCP has been set to 1120 V. The intensity distribution of the positrons released by Ps photoionization vs laser-pulse delays was thus acquired. Using the known x position of the Ps origin, the obtained distribution can be converted to a discrete velocity distribution along the x axis, v_x .

(ii) The Doppler scans [20,27] are performed in order to determine the Ps-velocity distribution parallel to the target, i.e., v_y . These scans were performed for fixed laser delays (once 23 ns and 31 ns for a second series), but with linearly adjustable UV wavelength between 204.900 nm and 205.200 nm in steps of 0.005 nm. Like this, one can investigate the $1^3S \rightarrow 3^3P$ transition in the vicinity of resonance. The IR laser was again set to 1064 nm as for (i) in order to produce photopositrons.

(iii) The self-ionization scans reveal the fraction of Rydberg-Ps surviving the magnetically induced motional Stark field as a function of the effective principal quantum number n_{eff} , a quantum number characterizing the Rydberg states in fields that will be defined later. These scans were done by changing the IR wavelength that is inducing the transition from $3^3P \rightarrow$ Rydberg. It was tuned from 1671 nm to 1715 nm, addressing effective Rydberg states between 14 and 22, while the UV laser was kept unchanged and at the reference wavelength. Both laser pulses were synchronously delayed by 25 ns. The internal MCP gain voltage was increased to 1200 V in order to be more sensitive to the emerging positrons from self-ionization effects. This enhancement of sensitivity is necessary because a low-intensity signal is expected for Ps self-ionization at higher IR wavelengths. The intensity of the image on the MCP was thus acquired as a function of the effective n state of Ps.

III. RESULTS AND DISCUSSION

The measurements produce a photopositron-induced image on the MCP+phosphor screen assembly, acquired by a CMOS camera (Hamamatsu C11440-22CU). An example for a signal after photoionization is shown in Fig. 2. One can see the ionized positronium cloud (red), emerging from below the border of the target. Note that here for visual verification of the internal alignment, the image was overlaid with an electron image (green), where the MCP frontface was charged with $+180$ V, which attracted, in turn, photoelectrons released from all surfaces after irradiation with the UV laser [28]. As a result, one can see the target border plus its holder on the top and the MACORscreen on the left. The laser approaches from the right in this view. The back of the target also seems to emit photoelectrons, which we attribute to multiple scattering of the UV laser. For analysis, only the positron image was taken into account.

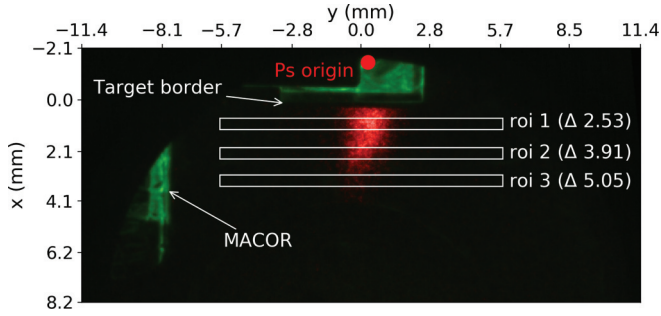


FIG. 2. Combination of an electron reference image (green) and a Ps-photoionization image (red): Positronium is emerging from the target border and gets instantaneously ionized when the laser pulses are sent. Unbound positrons are then guided towards the MCP, producing a light spot. We define regions of interest (*roi 1*, *roi 2*, *roi 3*), which have a width of 20 pixels (0.46 mm) and a length of 500 pixels (11.5 mm). The window *roi 1* is 2.53 mm away from the Ps origin, *roi 2* 3.91 mm and *roi 3* 5.05 mm. We sum all the intensities within the windows and subtract a background obtained from the averaged signal of the last six delays where no Ps photoionization could be observed.

The transverse spatial profile and energy distribution of both laser pulses, which are well described by a Gaussian, determine the absolute amount of ionized, and thus detectable, Ps atoms. A fraction of the photoreleased positrons, constrained to move along the magnetic field lines in the z direction, is hidden behind the target, the holder, or just out of the MCP range, and is therefore not available for the analysis. The UV beam has a full width at half maximum (FWHM) of approximately 4.4 mm, which at the same time defines the border of a sufficiently high fluence guaranteeing saturation of the Ps excitation across the illuminated surface [21]. The FWHM of the IR laser is $\sim 4\text{--}5$ mm. For analysis, we choose several rather narrow windows in the x - y plane on the MCP image, of which we will present three specific ones labeled *roi 1*, *roi 2*, and *roi 3* in Fig. 2. The windows have an extent of 20×500 pixels ($0.46 \times 11.5 \mu\text{m}$) and cover the visible region of 5 mm along the x axis. For each *roi*, the integrated signal of ionized Ps along the z axis depends on the geometrical overlap of the window with the laser beam at the instant of excitation. This implies that one can effectively compare different delays for the same *roi*, while other windows have different overall intensities. Generally, a narrow window is preferable since the broadness of it has an influence on how precise a specific velocity can be estimated in the case of timing scans. Furthermore, in the region close to the target border, edge effects (e.g., inhomogeneous fields) might influence the analysis.

As a first step in the experimental procedure, we had to correctly place the position of the positron beam incident on the converter, which we used as reference for the Ps origin. For this, we have measured the dimension of the positron spot in the center of the MCP, which was found to be 0.46 mm. We then have moved up the positron implantation point by adjusting the current of a vertical correction coil in the positron beam line, which did not influence the shape of the positron spot. A linear correlation of the vertical x coordinate and the current in the correction coil was observed. By means of this

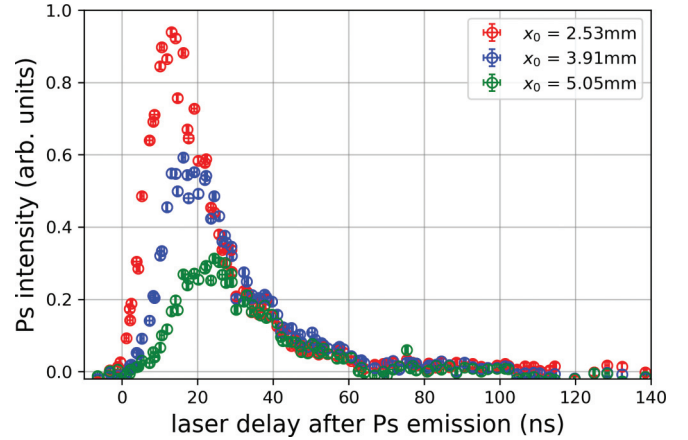


FIG. 3. Observed positronium intensity vs lasers delay for three different windows (*roi 1,2,3*). The distributions shift towards later times for more distant windows and, at the same time, decrease in intensity due to the limited geometrical overlap with the laser.

calibration, we were able to steer the positron implantation point to a fixed, hidden position on the positron-to-Ps converter target which serves as zero. The distances between this point and the center of *roi 1*, *roi 2*, and *roi 3* were found to be $x_0 = 2.53(38)$ mm, $3.91(38)$ mm, and $5.05(38)$ mm, respectively. The systematic errors on x_0 have been estimated by Gaussian error propagation, arising from the positron spot size (± 0.23 mm), the calibration measurement (± 0.2 mm), and the broadness of the analysis window (± 0.23 mm). The highest Ps flux has been assumed to originate from the center of the positron implantation spot.

A. Timing scans

The timing scans were repeated three times, so that an average image could be calculated for each delay. A background obtained from the averaged signal at very long delays with no evident photoionization signal was subtracted from the raw data points' amplitudes. We then obtain asymmetrical distributions displaying the intensities of observed Ps over different delays; see Fig. 3. After 140 ns, there is no longer any evident signal. We find that the distributions shift towards later times for windows that are more distant from the Ps origin, which is what one would expect. Furthermore, the peak intensities decrease with increasing distance, which is the net effect of the laser beam selecting a fraction of the expanding Ps cloud.

By using the relation $v_x = x_0/t$, we can translate the Ps time of flights (TOF) t into velocities using the distance x_0 between the Ps origin and the analysis windows introduced above. The velocity distributions were obtained by multiplying the observed Ps distributions of Fig. 3 with the term $t e^{t/142\text{ns}}$, i.e., by using the Jacobian determinant for converting the observed spatial distribution at different times into a velocity distribution and correcting for the natural decay of the ground-state ortho-Ps as is usually done for Ps-TOF measurements [29,30]. Different from these references, a single laser position was sufficient to resolve the velocity distribution in our highly magnetic environment, especially since a single MCP image provided many detection distances

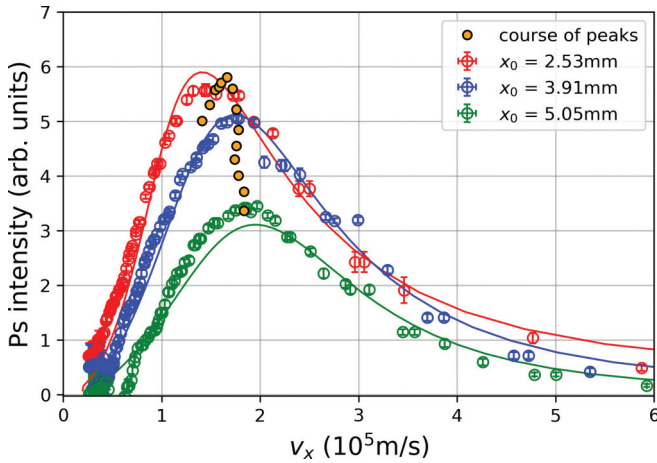


FIG. 4. Distribution of Ps velocities along the x axis as obtained from the timing scan of Fig. 3 after the treatment specified in the text. The solid lines are obtained from a simulation which is specified in the Appendix. The peak velocities have been marked with orange spots, not only for the defined analysis windows but also for additional windows with the same extent, sliding in steps of 10 pixel from the target border towards the trap electrodes.

x_0 at the same time. We then apply a sliding average in order to smooth the curves and increase the statistics, especially for the less intense low-velocity components (corresponding to long delays). The result is reported in Fig. 4. The solid lines are the outcome of a simulation aiming to qualitatively model the performed experiment (more details are given in the Appendix). All investigated distances result in a velocity distribution peaking between $1.4 \times 10^5 \text{ m s}^{-1}$ and $1.8 \times 10^5 \text{ m s}^{-1}$ (orange circles), where more distant windows have higher velocities.

We attribute this to a combination of two effects. The first is simply a geometrical effect because, for more distant *rois*, the contribution of Ps components aligned with the z axis is decreasing. As a consequence, the cleanest v_x distribution is obtained for the most distant window. The second effect is a permanence time of Ps in the nanochannels (t_{perma}) because, in reality, Ps emission from the nanochannels is not instantaneous [31]. The real Ps time of flight rather is $t_f = t - t_{\text{perma}}$, where t is the measured time elapsed from positron implantation to Ps ionization. The permanence time t_{perma} depends both on the positron implantation depth and the nanochannel diameter [22]. For closer *rois*, the presence of a permanence time yields a non-negligible overestimation of the generally smaller time of flights and, consequently, to an underestimation of Ps velocities. Increasing the *rois*' distance from the Ps origin minimizes this disturbing effect of the permanence time, rendering, together with the first effect, the most distant window to be the most trustworthy. In Fig. 4, we report the most probable velocity as a function of the *roi* distance (the course of the peaks) showing that the peak velocity stabilizes for distances greater than ~ 4 mm.

In light of this discussion, we use the velocity distribution obtained from the window at 5.05 mm (green curve in Fig. 4) as reference. It has its most frequent velocity component $v_{x,\text{max}}$ at $1.80(25) \times 10^5 \text{ m s}^{-1}$. The given error was derived

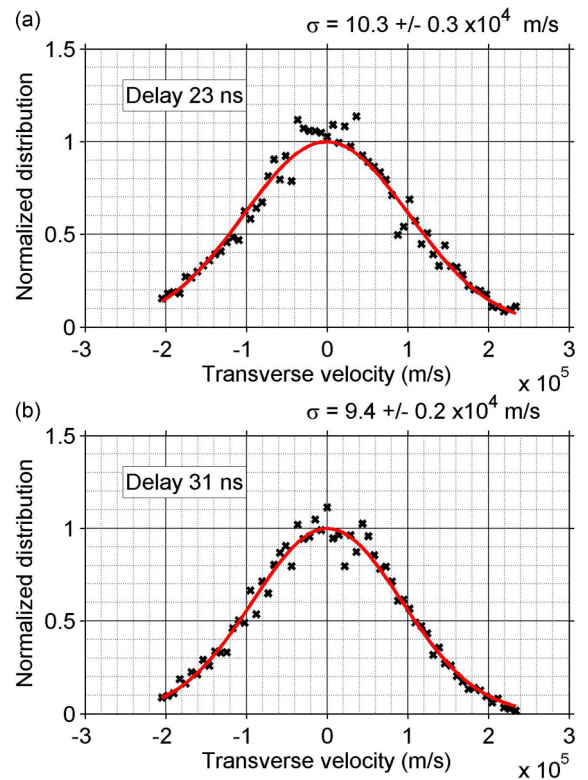


FIG. 5. (a) Doppler scan at 23 ns delay. (b) Doppler scan at 31 ns delay. Both distributions have a peak at $v_y = 0 \text{ m s}^{-1}$ corresponding to $\lambda = 205.045 \text{ nm}$.

from the width of the window that we used for the sliding average.

B. Doppler scans

The Doppler scans were repeated five times so that we could average the images per wavelength. The v_y distribution has been extracted from the photoionization images in the following way. Within the reference window *roi* 3, all intensity values of one averaged image have been summed up and a constant background, i.e., the average value of a region on the MCP image where no Ps can be photoionized, was subtracted. Repeating this for all wavelengths, one obtains the photoionization signal dependent on the UV-laser setting. Furthermore, the wavelength can directly be expressed as the Ps velocity component v_y propagating parallel or antiparallel to the laser beam by using the Doppler relation,

$$v_y = c \left(1 - \frac{\lambda}{\lambda_r} \right), \quad (2)$$

where c is the speed of light in vacuum and $\lambda_r = 205.045 \text{ nm}$ is the reference wavelength for the excitation of the $n = 3$ manifold in our experimental conditions. In Fig. 5, the summed intensities are shown as a function of the velocity v_y as well as Gaussian fits, from which the sigmas of the distributions have been extracted. Doppler scans strictly distinguish between velocities propagating towards the light source and those moving away from it. This is expressed by positive and negative velocities in Fig. 5, respectively. Note

that this measurement of the v_y distribution is independent of the result of timing scans, which led to the v_x distribution. Figure 5(a), with a laser delay of 23 ns, has a sigma of $1.03(3) \times 10^5 \text{ m s}^{-1}$. Figure 5(b), with a set delay of 31 ns, has a sigma of $0.94(2) \times 10^5 \text{ m s}^{-1}$. These velocities correspond to the mean velocity of the distribution aligned with the y axis. For the greater delay, the velocity spread of positronium being in the visible region on the MCP seems a bit decreased, which could be due to faster Ps components having moved out of view or due to nonisotropic Ps emission from the target.

The v_y distribution of this work is comparable to the one obtained for a similar target at room temperature reported in Ref. [20]. The absence of important differences in this temperature range can be ascribed to the rather low positron implantation energy and the relatively large nanochannel size of the converters used in both experiments. Indeed, in these experimental conditions, the number of interactions of Ps with the channels' walls before emission into vacuum is expected to be insufficient for a complete thermalization, which is why the target temperature has no strong influence on the results [22].

The best UV wavelength for the AEGIS setup is the one where the greatest fraction of Rydberg-Ps is moving towards the meshed grid at the top of the H-production trap. With the current alignment of laser, target, and trap, this is just the $v_y = 0$ component, i.e., $\lambda = \lambda_r$.

C. Self-ionization scan of Rydberg-Ps

Rydberg-Ps has a strong dipole moment scaling with the principal quantum number squared. Hence, it is sensibly affected by electric fields despite the general neutrality of Ps. This, on one hand, enables motional control, for example, via Stark deceleration as described in Ref. [32], but, on the other hand, it also puts constraints to its production in strong magnetic fields. In such, the motion of Rydberg-Ps induces an electrical field following $\vec{F}_{\text{mot}} = \vec{v} \times \vec{B}$. This is the so-called motional Stark effect and its strength depends on the velocity components perpendicular to the magnetic field. Here, this is only v_x because, with the laser set to resonance, we selected $v_y \approx 0 \text{ m s}^{-1}$. The presence of this electric field can cause self-ionization of the moving Ps atom. In particular, the minimal electric field causing ionization on some Ps states, usually called the *ionization threshold*, generally depends on a principal quantum number n [19,33] and can be written in our case as

$$F_{\text{limit}}(n) = \frac{E_{Ps}}{9ea_0} \frac{1}{n_{\text{eff}}^4}. \quad (3)$$

Here, E_{Ps} is the Rydberg energy for the positronium (equal to 6.8 eV), e is the electric charge, and a_0 is the standard Bohr radius, while n_{eff} represents an effective quantum number depending only on the wavelength λ characterizing the $n = 3 \rightarrow$ Rydberg transition through the well-established Rydberg formula for hydrogenlike systems,

$$\frac{hc}{\lambda} = E_{Ps} \left[\frac{1}{(n=3)^2} - \frac{1}{n_{\text{eff}}^2} \right]. \quad (4)$$

This reformulation is possible since the distribution of Ps-Rydberg states resembles a continuum rather than well-

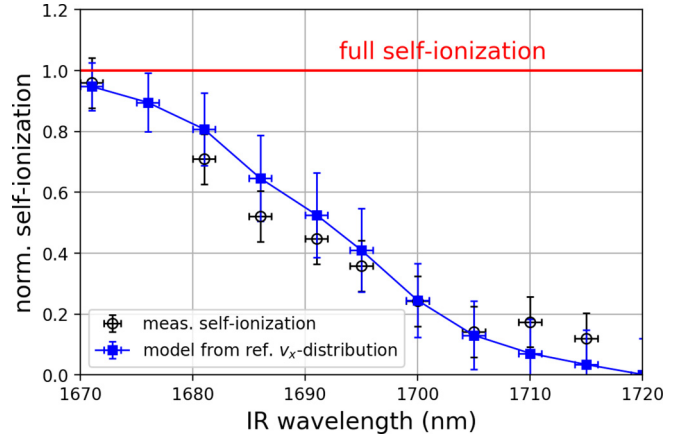


FIG. 6. IR-wavelength scan corresponding to Ps-Rydberg states (circles with error bars). The self-ionizing fractions have been normalized to the expected full self-ionization. For $\lambda = 1680 \text{ nm}$, around 70% of Ps ionizes. At $\lambda = 1700 \text{ nm}$, which corresponds to $n_{\text{eff}} \approx 16$, only 25% is lost. The squares are the result of a modeling of the self-ionizing fraction, as detailed in the text. The model resembles the measured self-ionization per effective state.

separated single states as the classical formula would imply. In fact, the presence of the motional Stark effect is highly relevant for Rydberg-excited Ps atoms: it destroys the axial symmetry and determines, via mixing of ℓ and m substates, the spread of energy levels for the n manifold. It also determines the interleaving of nearby n manifolds, finally leading to a quasicontinuum structure of energy levels [19,34]. This also has the consequence that the efficiency of the transition $n = 3 \rightarrow$ Rydberg is essentially dominated by the IR-laser bandwidth of 430 GHz.

By using the relation in Eq. (4), one finally obtains the self-ionization limit as a function of the IR-excitation wavelength λ ,

$$F_{\text{limit}}(\lambda) = \frac{E_{Ps}}{9ea_0} \left(\frac{1}{9} - \frac{hc}{E_{Ps}\lambda} \right)^2, \quad (5)$$

and from the relation $v_{x,\text{limit}} = F_{\text{limit}}/B$, with $B = 1 \text{ T}$, the corresponding limiting velocity that is used in the following analysis of experimental data.

Also, in the case of Rydberg-Ps self-ionization, produced positrons can be imaged on the MCP, although the number of detectable particles turns out generally smaller. Therefore, unlike before, we used a larger analysis window ranging from the target border to *roi* 3 for a better signal intensity, and normalized it with the corresponding signal from the measurement at the lowest possible wavelength ($\lambda = 1671 \text{ nm}$). At the same time, one can calculate the effective ionization threshold for this lowest wavelength by using Eq. (5), which gives $6 \times 10^4 \text{ m s}^{-1}$. Integrating the reference v_x -velocity distribution found in the previous paragraph for all values that are greater than this threshold and normalizing the result to the total integral, one obtains an estimate for the maximum expected self-ionization signal which resulted in 97%.

The outcome of a self-ionization scan for a fixed delay of 25 ns and for the UV-laser set to our reference wavelength is shown in Fig. 6 (circles with error bars). For $\lambda =$

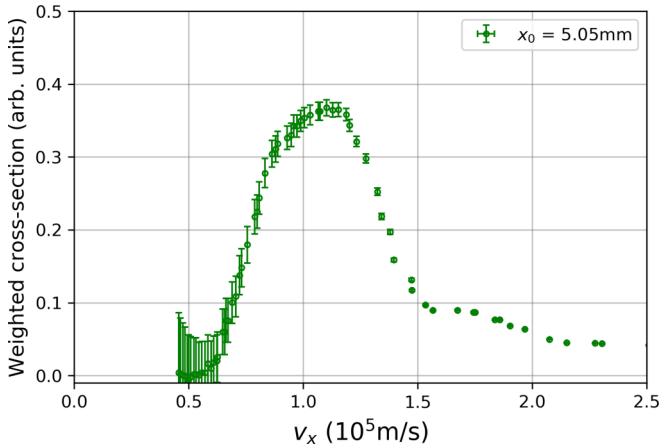


FIG. 7. Weighted cross section for antihydrogen production using Rydberg-Ps with $\lambda_{IR} = 1700$ nm, plotted over the whole accessible range of Ps velocities along the x axis.

1700 nm (i.e., $n_{\text{eff}} \approx 16$), only about 25% ionizes, and thus this state seems a reasonable choice when optimizing the charge-exchange reaction, as the visible self-ionizing Ps is still very dim, while n_{eff} is not too small.

The velocimetry result of Fig. 4 obtained for the window at 5.05 mm has been used to model the self-ionizing fraction of Rydberg-Ps. For each IR wavelength, the threshold of self-ionization and the corresponding limiting velocity $v_{x,\text{limit}}$ have been calculated from Eq. (5). Then, the fraction of self-ionizing positronium has been computed via numerical integration: all bins with a velocity higher than the ionization limit contribute to a signal, which is normalized to the result of an integration over all velocities. The model (squares with error bars) is plotted together with the measured self-ionization over the wavelengths in Fig. 6. The model roughly follows the course of the measured self-ionization, which is an indication for the quality of the velocity distribution along the x axis.

D. Expected impact on the $\bar{\text{H}}$ -production cross section

The cross section for $\bar{\text{H}}$ -production via the charge-exchange reaction was studied theoretically by different groups. Classical simulations [18] based on Monte Carlo numerical experiments have given insight into the process for Rydberg states up to $n = 50$. Quantum effects have also been studied in simulations up to $n = 5$, but subsequent investigations have pointed out that the scaling laws are identical [35,36]. Within the framework of the classical Monte Carlo approach, the predicted cross section gets larger with increasing Ps principal quantum number n (proportional to n^2 at very small velocities and to n^4 at intermediate ones), and decreases monotonically with the Ps velocity, becoming negligible at the fast end.

By using these studies, one can optimize the described Rydberg-Ps source for future efficient antihydrogen production in AEGIS. For this purpose, we weighted the classical cross section with the measured reference v_x -velocity distribution of Ps. This has been done for all accessible IR wavelengths. The result for $\lambda_{IR} = 1700$ nm is shown in Fig. 7. The weighted cross section shows a plateau in the region

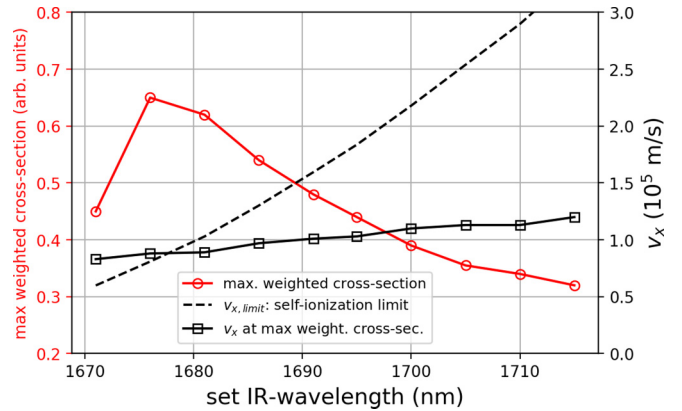


FIG. 8. Left ordinate: maximum of the weighted cross sections. Right ordinate: the vertical velocity component v_x . Both are plotted over the set IR-laser wavelength addressing the effective Rydberg state. The solid lines are meant as guides for the eye, while the dashed line represents the limiting velocity of self-ionization.

of $1 \times 10^5 \text{ m s}^{-1}$, which is due to the strong suppression of faster components, where the relative velocity between Ps and antiprotons is mismatched. When properly tuning the laser pulses' delay and thus the selected range of velocities, one can maximize the weighted cross section (with an optimal velocity v_{best}). More so, as it is expected to progressively increase with decreasing λ_{IR} .

If v_{best} is smaller than the limiting velocity $v_{x,\text{limit}}$ for a given IR wavelength, it is convenient to address the positronium with that velocity to have the highest weighted cross section for $\bar{\text{H}}$ -production. On the other side, if v_{best} is greater than the limiting velocity, the positronium traveling with that velocity would self-ionize and cannot be used. In this case, Ps with a velocity regime slightly before the limit should be addressed by an appropriate choice of laser delay.

In Fig. 8, the behavior of v_{best} and of $v_{x,\text{limit}}$ is shown as a function of the IR wavelength. For $\lambda_{IR} \geq 1680$ nm, v_{best} is lower than $v_{x,\text{limit}}$. For example, the weighted cross section gains roughly a factor of two when going from (1700–1676) nm with our Ps source, despite the dramatic increase in self-ionization. The improvement originates from the scaling of the surviving fraction with n^4 . Additionally, when optimizing the positron implantation energy or possibly the morphology of the target itself, one could obtain a slower Ps velocity distribution, which potentially allows one to reduce the wavelength even more as the self-ionizing fraction is reduced.

IV. CONCLUSIONS

In this work, we have characterized the velocity emission of positronium from a nanochanneled positron-to-positronium converter in a cryogenic environment within a magnetic field of 1 T. The self-ionization of positronium due to the motional Stark effect has also been studied as a function of the wavelength of the IR laser exciting Ps-to-Rydberg states, with an effective principal quantum number n_{eff} ranging between 14 and 22. The measurements have been performed by means of MCP imaging of ionized positronium. In the case of velocimetry, positronium was photoionized after excitation,

while for the study of the motional Stark effect, self-ionized Rydberg positronium has been imaged. The velocimetry was performed for two axes. The velocity components aligned parallel to the laser beam have been studied by Doppler scanning the UV wavelength populating the $n = 3$ manifold; the velocity components perpendicular to the laser and to the magnetic field were measured by timing scans of the delays for the laser pulses. The choice of the positronium velocity and Rydberg state of the atom has been discussed in view of their optimization for \bar{H} -production via charge-exchange reaction.

ACKNOWLEDGMENTS

This work was supported by the Istituto Nazionale di Fisica Nucleare; the CERN Fellowship programme and the CERN Doctoral student programme; the Swiss National Science Foundation Ambizione (Grant No. 154833); a Deutsche Forschungsgemeinschaft research grant; an excellence initiative of Heidelberg University; Marie Skłodowska-Curie Innovative Training Network Fellowship of the European Commission's Horizon 2020 Programme (Grant No. 721559 AVA); European Research Council under the European Unions Seventh Framework Program FP7/2007-2013 (Grants No. 291242 and No. 277762); European Union's Horizon 2020 research and innovation programme under the Marie Skłodowska-Curie Grant Agreement ANGRAM No. 748826; Austrian Ministry for Science, Research, and Economy; Research Council of Norway; Bergen Research Foundation; John Templeton Foundation; Big&Open Data Innovation Laboratory (BODaI-Lab), University of Brescia, granted by Fondazione Cariplo and Regione Lombardia; and the Ministry of Education and Science of the Russian Federation and Russian Academy of Sciences and the European Social Fund within the framework of realizing research infrastructure for experiments at CERN, LM2015058.

APPENDIX: MODELING OF THE PS v_x DISTRIBUTION

We consider a positron bunch impacting and entering the positron-to-Ps converter at the reference position $(0, 0, 0)$ of our coordinate system and assign a temporal spread modeled by a normalized Gaussian function centered at time $t = 0$ to it,

$$n_p(t) = \frac{1}{\sigma_p \sqrt{2\pi}} e^{-t^2/2\sigma_p^2}. \quad (\text{A1})$$

For σ_p , we assume a value of 5 ns as was estimated from the experimental data. Every positron in the bunch is then assumed to form Ps, which exits the converter from the reference point after an averaged Ps permanence time t_{perma} inside the target. Hence, we get an initial Ps cloud with the same time distribution as the positron bunch, but centered at $t = t_{\text{perma}}$. We then also define a velocity distribution function $f_0(v_x, v_y, v_z)$ for the Ps cloud, which we model with a Gaussian function as well, centered at $v_{x,y,z} = 0 \text{ m s}^{-1}$.

The possible resulting velocity vectors are limited to an emission cone with its vertex located at the Ps origin and a half opening angle θ from the target normal (see Fig. 9). The Ps cloud is freely expanding in space obeying the linear law,

$$x(t_f) = v_x t_f, \quad y(t_f) = v_y t_f, \quad z(t_f) = v_z t_f, \quad (\text{A2})$$

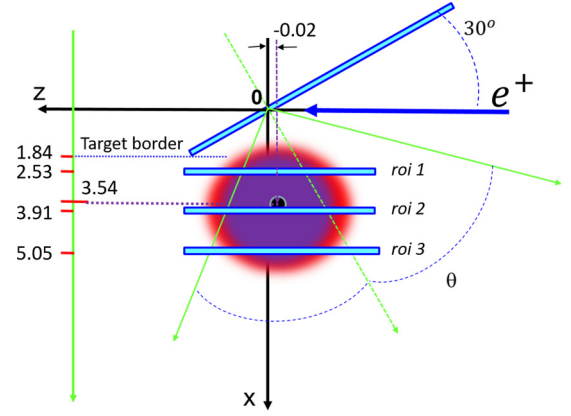


FIG. 9. Geometry used for the modeling of Ps photoionization with the three *rois* 1,2,3 as used during the experimental analysis. See Table I for a summary of position coordinates and dimensions.

where t_f is the real Ps flight time. We can therefore describe the Ps cloud by a spatial distribution function $f(x(t_f), y(t_f), z(t_f))$ within the emission cone. By equating the number of Ps contained in a spatial volume element $dx dy dz$ with the number of Ps contained in a velocity volume element $dv_x dv_y dv_z$, we can express the spatial distribution in terms of the initial velocity distribution f_0 for each time $t_f > 0$,

$$f(x, y, z) dx dy dz = f_0(v_x, v_y, v_z) dv_x dv_y dv_z \\ \Rightarrow f(x, y, z) = \frac{1}{t_f^3} f_0(v_x, v_y, v_z). \quad (\text{A3})$$

During their free flight in vacuum, Ps atoms can be probed by two synchronized and spatially overlapped laser pulses (UV+IR, aligned with the y axis) by means of an initial excitation to $n = 3$ and a subsequent ionization, which we assume for practical reasons to work instantaneously. The instant of laser firing corresponds to a time $t = t_f + t_{\text{perma}}$. The laser-beam profiles are assumed to be Gaussian transverse functions centered in (x_L, z_L) , and with $2\Delta r$ as FWHM. We define a

TABLE I. Experimental and assumed parameters for the simulation.

Δx	0.46 mm	<i>roi</i> width along x
Δy	11.5 mm	<i>roi</i> width along y
x_1	2.53 mm	center of <i>roi</i> 1
x_2	3.91 mm	center of <i>roi</i> 2
x_3	5.05 mm	center of <i>roi</i> 3
x_L	3.54 mm	x position of laser center
z_L	-0.02 mm	z position of laser center
Δr	2.2 mm	laser spot FWHM
g_1	0.55	efficiency of Ps ionization in <i>roi</i> 1
g_2	0.62	efficiency of Ps ionization in <i>roi</i> 2
g_3	0.53	efficiency of Ps ionization in <i>roi</i> 3
θ	60°	half opening angle of Ps emission
σ_p	5 ns	temporal spread of e^+ bunch
σ_v	$2 \times 10^5 \text{ m s}^{-1}$	velocity spread of Ps cloud
t_{perma}	3 ns	Ps permanence time

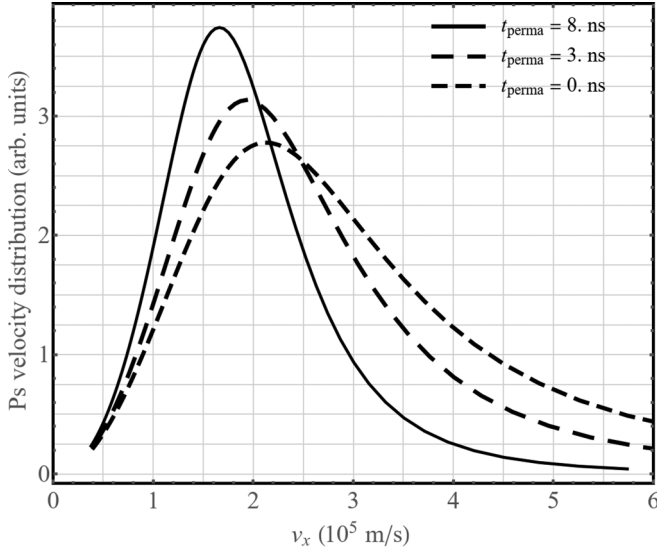


FIG. 10. Variance of the modeled v_x -velocity distribution for a reasonable range of permanence times t_{perma} in *roi* 3.

function $\chi_{\text{cone}}(\theta)$, which is describing the overlap of the Ps emission cone and the laser beam. If θ is sufficiently large, which is the case for $\theta \geq 60^\circ$, then the function $\chi_{\text{cone}}(\theta) = 1$.

The number of detected ionized Ps atoms in the *roi* centered at x_r at observation time t is given by a spatial integral:

$$N_r(t) \equiv N_r(t_f + t_p) = g_r \int_{x_r - \Delta x/2}^{x_r + \Delta x/2} dx \int_{-\Delta y/2}^{\Delta y/2} dy \times \int_{z_L - \Delta z}^{z_L + \Delta z} dz \chi_{\text{cone}}(\theta) \times f(x(t_f), y(t_f), z(t_f)), \quad (\text{A4})$$

where g_r is the efficiency of ionization as was calculated following the procedure described in Ref. [19]. The slightly varying values for $g_{1,2,3}$ as given in Table I are due to the geometrical overlap of the *rois* with the Gaussian spatial laser profile, which at the same time is defining the third integral's boundary, Δz , via the Pythagorean theorem,

$$\Delta z = \sqrt{\Delta r^2 - (x_r - x_L)^2} \begin{cases} \Delta z & \text{for } |x_r - x_L| \leq \Delta r \\ 0 & \text{for } |x_r - x_L| > \Delta r. \end{cases} \quad (\text{A5})$$

From the distribution $N_r(t)$, which is a small excerpt from the initial spatial distribution, we can derive the measurable v_x -velocity distribution $P_r(v_x)$ with a simple procedure using

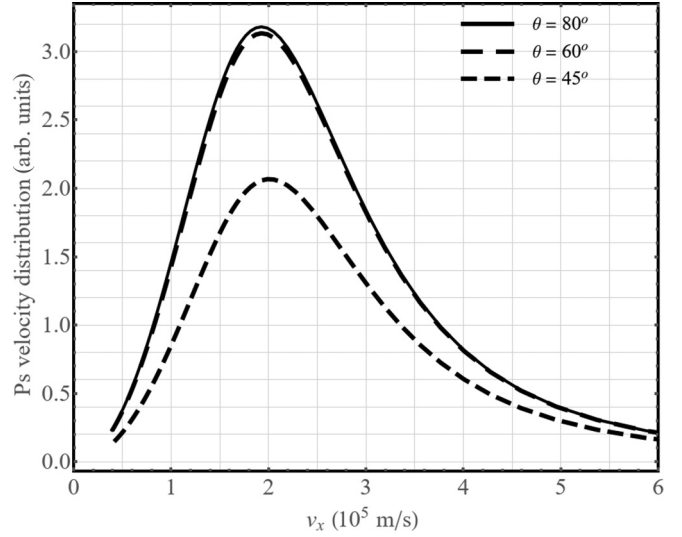


FIG. 11. Dependence of the modeled v_x -velocity distribution on the Ps emission cone defined by θ in *roi* 3.

the above definitions,

$$\begin{aligned} P_r(v_x) &\equiv \int dv_y dv_z f_0(v_x, v_y, v_z) \\ &= \frac{1}{t_f^2} \int dy dz f_0(v_x, v_y, v_z) \\ &= t_f \int dy dz f(x(t_f), y(t_f), z(t_f)). \end{aligned}$$

Assuming, as before, a sufficiently large Ps emission cone, the integrals are limited by the *rois*' width Δx and by the laser-beam profile, and, with Eq. (A4), we finally obtain the formula

$$P_r(v_x) \simeq \frac{t_f}{g_r \Delta x} N_r(t). \quad (\text{A6})$$

The approximate simulations reported in Fig. 4 have been obtained using the parameters in Table I. We show the influence of the parameters t_{perma} and θ in Fig. 10 and Fig. 11, where a reasonable range has been explored for our reference *roi* 3. The Ps intensity varies less and the peak velocity more when changing the permanence time t_{perma} . As the velocities directly depend on the real time of flight, this strong correlation is expected. Varying the Ps emission cone, for angles greater than 60° , no change occurs because the laser beam is fully overlapping with the Ps cloud. Reducing that angle, the amplitude decreases rapidly while the peak velocity slightly increases.

- [1] P. A. M. Dirac, *Proc. R. Soc. London A* **126**, 360 (1930).
 [2] C. D. Anderson, *Phys. Rev.* **43**, 491 (1933).
 [3] S. Mohorovičić, *Astron. Nachr.* **253**, 93 (1934).
 [4] M. Deutsch, *Phys. Rev.* **82**, 455 (1951).
 [5] A. I. Alekseev, *ZhETF* **34**, 1195 (1958) [*Sov. Phys. JETP* **7**, 826 (1958)].
 [6] A. I. Alekseev, *ZhETF* **36**, 1839 (1959) [*Sov. Phys. JETP* **9**, 1312 (1959)].

- [7] W. E. Caswell and G. P. Lepage, *Phys. Rev. A* **20**, 36 (1979).
 [8] D. B. Cassidy, T. H. Hisakado, H. W. K. Tom, and A. P. Mills, Jr., *Phys. Rev. Lett.* **106**, 133401 (2011).
 [9] D. B. Cassidy, T. H. Hisakado, H. W. K. Tom, and A. P. Mills, Jr., *Phys. Rev. Lett.* **109**, 073401 (2012).
 [10] S. Aghion, C. Amsler, M. Antonello, A. Belov, G. Bonomi, R. S. Brusa, M. Caccia, A. Camper, R. Caravita, F. Castelli *et al.* (AEGIS collaboration), *Phys. Rev. A* **98**, 013402 (2018).

- [11] S. Chu and A. P. Mills, Jr., *Phys. Rev. Lett.* **48**, 1333 (1982).
- [12] D. B. Cassidy, *Eur. Phys. J. D* **72**, 53 (2018).
- [13] G. Baur, G. Boero, A. Brauksiepe, A. Buzzo, W. Eyrich, R. Geyer, D. Grzonka, J. Hauffe, K. Kilian, M. LoVetere *et al.* (LEAR collaboration), *Phys. Lett. B* **368**, 251 (1996).
- [14] M. Amoretti, C. Amsler, G. Bonomi, A. Bouchta, P. Bowe, C. Carraro, C. L. Cesar, M. Charlton, M. J. T. Collier, M. Doser *et al.* (ATHENA collaboration), *Nature (London)* **419**, 456 (2002).
- [15] G. Gabrielse, N. S. Bowden, P. Oxley, A. Speck, C. H. Storry, J. N. Tan, M. Wessels, D. Grzonka, W. Oelert, G. Schepers *et al.* (ATRAP collaboration), *Phys. Rev. Lett.* **89**, 213401 (2002).
- [16] Scientific Committee Paper, ERN-SPSC-2019-007; SPSC-SR-246 <https://cds.cern.ch/record/2654355?ln=de>.
- [17] M. Charlton, *Phys. Lett. A* **143**, 143 (1990).
- [18] D. Krasnický, R. Caravita, C. Canali, and G. Testera, *Phys. Rev. A* **94**, 022714 (2016).
- [19] F. Castelli, I. Boscolo, S. Cialdi, M. G. Giammarchi, and D. Comparat, *Phys. Rev. A* **78**, 052512 (2008).
- [20] S. Aghion, C. Amsler, A. Ariga, T. Ariga, G. Bonomi, P. Bräunig, J. Bremer, R. S. Brusa, L. Cabaret, M. Caccia *et al.* (AEgIS collaboration), *Phys. Rev. A* **94**, 012507 (2016).
- [21] C. Amsler, M. Antonello, A. Belov, G. Bonomi, R. S. Brusa, M. Caccia, A. Camper, R. Caravita, F. Castelli, G. Cerchiari *et al.* (AEgIS collaboration), *Nucl. Instrum. Methods B* **457**, 44 (2019).
- [22] S. Mariazzi, P. Bettotti, and R. S. Brusa, *Phys. Rev. Lett.* **104**, 243401 (2010).
- [23] R. Caravita, S. Mariazzi, S. Aghion, C. Amsler, M. Antonello, A. Belov, G. Bonomi, R. S. Brusa, M. Caccia, A. Camper *et al.* (AEgIS collaboration), *AIP Conf. Proc.* **2182**, 030002 (2019).
- [24] B. S. Cooper, A. M. Alonso, A. Deller, L. Liskay, and D. B. Cassidy, *Phys. Rev. B* **93**, 125305 (2016).
- [25] S. Aghion, C. Amsler, A. Ariga, T. Ariga, A. S. Belov, G. Bonomie, P. Bräunig, J. Bremer, R. S. Brusa, L. Cabaret *et al.* (AEgIS collaboration), *Nucl. Instrum. Methods B* **362**, 86 (2015).
- [26] R. Caravita, M. Antonello, A. Belov, G. Bonomi, R. S. Brusa, M. Caccia, A. Camper, F. Castelli, G. Cerchiari, D. Comparat *et al.* (AEgIS collaboration), *Acta Phys. Pol. A* **137**, 96 (2020).
- [27] D. B. Cassidy, P. Crivelli, T. H. Hisakado, L. Liskay, V. E. Meline, P. Perez, H. W. K. Tom, and A. P. Mills, Jr., *Phys. Rev. A* **81**, 012715 (2010).
- [28] A. Camper, S. Aghion, C. Amsler, M. Antonello, A. Belov, G. Bonomi, R. S. Brusa, M. Caccia, R. Caravita, F. Castelli *et al.* (AEgIS collaboration), *EPJ Web Conf.* **198**, 00004 (2019).
- [29] R. H. Howell, I. J. Rosenberg, M. J. Fluss, R. E. Goldberg, and R. B. Laughlin, *Phys. Rev. B* **35**, 5303 (1987).
- [30] A. Deller, B. S. Cooper, T. E. Wall, and D. B. Cassidy, *New J. Phys.* **17**, 043059 (2015).
- [31] D. B. Cassidy, T. H. Hisakado, V. E. Meline, H. W. K. Tom, and A. P. Mills Jr., *Phys. Rev. A* **82**, 052511 (2010).
- [32] S. D. Hogan, *EPJ Tech. Instr.* **3**, 2 (2016).
- [33] T. F. Gallagher, *Rydberg Atoms*, Cambridge Monographs on Atomic, Molecular and Chemical Physics (Cambridge University Press, Cambridge, 1994).
- [34] F. Castelli, *Eur. Phys. J.: Spec. Top.* **203**, 137 (2012).
- [35] A. S. Kadyrov, I. Bray, M. Charlton, and I. I. Fabrikant, *Nat. Commun.* **8**, 1544 (2017).
- [36] D. Krasnický, G. Testera, and N. Zurlo, *J. Phys. B: At. Mol. Opt. Phys* **52**, 115202 (2019).